Near-Infrared Electroluminescent Light-Emitting Transistors Based on CVD-Synthesized Ambipolar ReSe₂ Nanosheets

Roshan Jesus Mathew, Kai-Hsiang Cheng, Ching-Hong Hsu, Pradyumna Kumar Chand, Christy Roshini Paul Inbaraj, Yu-Lou Peng, Jung-Yen Yang, Chih-Hao Lee, and Yit-Tsong Chen*

Near-infrared light-emitting technology is ideal for noncontact diagnostic medical imaging and high-speed data communications. High-quality ReSe₂ nanosheets of anisotropic single-crystal structure with a bandgap of 1.26 eV (≈984 nm) are synthesized with an atmospheric pressure chemical vapor deposition (APCVD) method. The as-synthesized ReSe₂ nanosheets-fabricated light-emitting transistors (LETs) exhibit nearly symmetric ambipolar characteristics in electrical transport. Judicious selection of asymmetric platinum (Pt)/chromium (Cr) electrodes, with their work functions matching respectively the conduction- and valence-band edges of ambipolar ReSe₂, generates a low turn-on voltage ReSe₂-LET with the balanced number density and field-effect mobility of bipolar carriers (i.e., electrons and holes). Room-temperature near-infrared electroluminescence (NIR EL) from the frequency-modulated ReSe₂-LET has been observed unprecedentedly with the assistance of a lock-in detection system. The NIR EL intensity is tested by varying the bias voltage applied to the ReSe₂-LET devices with different channel lengths. The wavelength of the NIR EL from ReSe₂-LET is differentiated with optical band-pass filters. Room-temperature angle-dependent two lobe-shaped EL pattern manifests the inherent anisotropic in-plane excitonic polarization of the ReSe₂ crystal. The highly stable NIR EL from ReSe₂-LETs provides prospective 2D material-based ultrathin scalable data communication electronics for future development.

1. Introduction

Transition metal dichalcogenides (TMDs) with their diverse electrical and optical properties[1] as emerging materials for electroluminescent devices have attracted significant research attention in optoelectronics.[2] A *p-n* junction-based traditional light-emitting diode (LED), consisting of a stacked pair of *p*-type (hole dominant) and *n*-type (electron dominant) unipolar semiconductors, can be formed by chemical doping,[3] electrostatic gating,[4,5] or van der Waals heterostructures.[6,7] The recombination of holes and electrons at the *p-n* junction interface leads to light emission through exciton annihilation.[8,9] In such *p-n* junction-based LEDs, imbalanced concentrations between the bipolar carriers (i.e., electrons and holes) could cause a wide depletion barrier at the junction interface,[10,11] resulting in hindering electron-hole recombination and limiting device performance. Moreover, a high bias voltage (V_b) required to drive the minority charge carriers in a device could move the recombination zone toward the vicinity of the electrode to quench the majority charge carriers without effectual recombination.[12–14]

In contrast, a light-emitting transistor (LET) can integrate the electroluminescence (EL) capability of LEDs and the electrical switching and amplification properties of transistors in a single device. In particular, the LET with its conducting channel comprising only a single-component ambipolar material can hold a highly dense, balanced concentrations of bipolar carriers.

R. J. Mathew, K.-H. Cheng, Y.-T. Chen
Institute of Atomic and Molecular Sciences
Academia Sinica
Taipei 10617, Taiwan
E-mail: ytcchem@ntu.edu.tw
R. J. Mathew
Nano-Science and Technology Program
Taiwan International Graduate Program
Academia Sinica
Taipei 11529, Taiwan

The ORCID identification number(s) for the author(s) of this article can be found under https://doi.org/10.1002/adom.202102580.

R. J. Mathew, C.-H. Lee
Department of Engineering and System Science
National Tsing-Hua University
Hsinchu 30013, Taiwan
K.-H. Cheng, C.-H. Hsu, P. K. Chand, Y.-L. Peng, Y.-T. Chen
Department of Chemistry
National Taiwan University
Taipei 10617, Taiwan
C. R. Paul Inbaraj
Department of Physics
National Taiwan University
Taipei 10617, Taiwan
J.-Y. Yang
National Applied Research Laboratories
Taiwan Semiconductor Research Institute
Hsinchu 30078, Taiwan

With a simple planar geometry design, this single-component ambipolar LET with the balanced injection of bipolar carriers to the same conducting channel will not only emit light through exciton annihilation, but also modulate the recombination zone between the source and drain electrodes.[15–18] Moreover, an ambipolar LET device with a dense accumulation of bipolar carriers could suppress the quenching of holes or electrons at the vicinity of the electrode, thereby enhancing optoelectronic quantum efficiency and reducing manufacturing complexity for prospective development.[14,18] Consequently, ambipolar LETs enabling the spatially controllable light emission pave a new avenue to study the excitonic effects for integrated optoelectronic devices.

In the development of ambipolar LET devices, the single-component active layers were explored earlier by employing organic materials and inspected recently with TMDs. In early studies on single-component ambipolar organic LETs, the solution-processed PPV thin films[19] of OC_1C_{10}-PPV[20] and F8BT[21] were used as the conducting channels. Later, ambipolar organic LETs were achieved with single-crystalline tetracene, pentacene, and rubrene active layers.[22–24] On the other hand, TMDs-based single-component ambipolar LETs, despite rare studies, were investigated lately with either the electrolyte-gated or split-gate geometry. To date, the EL emitted from TMDs-based LETs has been observed in the ionic liquid-gated monolayer and bilayer WS_2, large-area MoS_2 films,[25] few-layer WSe_2,[26] thin $MoSe_2$ flakes,[27] and thick ReS_2 flakes.[28] Meanwhile, a lateral *p-n* homojunction created electrostatically by applying two independent gate-voltages to an ambipolar WSe_2 monolayer was also examined to illuminate at 752 nm in ambient conditions.[29,30] However, the ambipolar characteristic of WSe_2 is restricted only to its monolayer crystal, hindering the scalable sample preparation.

Alternatively, the $ReSe_2$ nanosheets of a distorted triclinic crystal structure with prominent electrical and optical properties represent another promising 2D material with ambipolar transport characteristics.[31,32] Thin-layered $ReSe_2$ crystal can be synthesized with a chemical vapor deposition (CVD) method.[33] Unlike WSe_2,[34] the bandgap of $ReSe_2$ has little dependence on the crystal thickness and was reported to be 1.3 eV for the monolayer and 1.1 eV for multilayers.[32,35] Moreover, the electrical transport of a $ReSe_2$-based transistor can be modulated to be electron- or hole-dominant by contact electrode engineering.[33] Despite several recent studies revealing the electrical and optical characteristics of the $ReSe_2$ crystal, the EL from a $ReSe_2$-LET has not yet been explored to highlight its inherent ambipolar nature. In this study, we demonstrate that near-infrared (NIR) EL can be emitted from an ambipolar $ReSe_2$-LET in ambient conditions. Distinct from the aforementioned TMD-based ambipolar devices via the electrolyte-gated or split-gate design,[25–30] the conducting channel of the ambipolar $ReSe_2$ nanosheets in our $ReSe_2$-LET devices was electrically connected to a pair of asymmetric platinum (Pt)/chromium (Cr) electrodes, which were selected to reduce the Fermi level pinning (FLP) for a balanced injection of bipolar carriers to achieve optimal NIR EL.
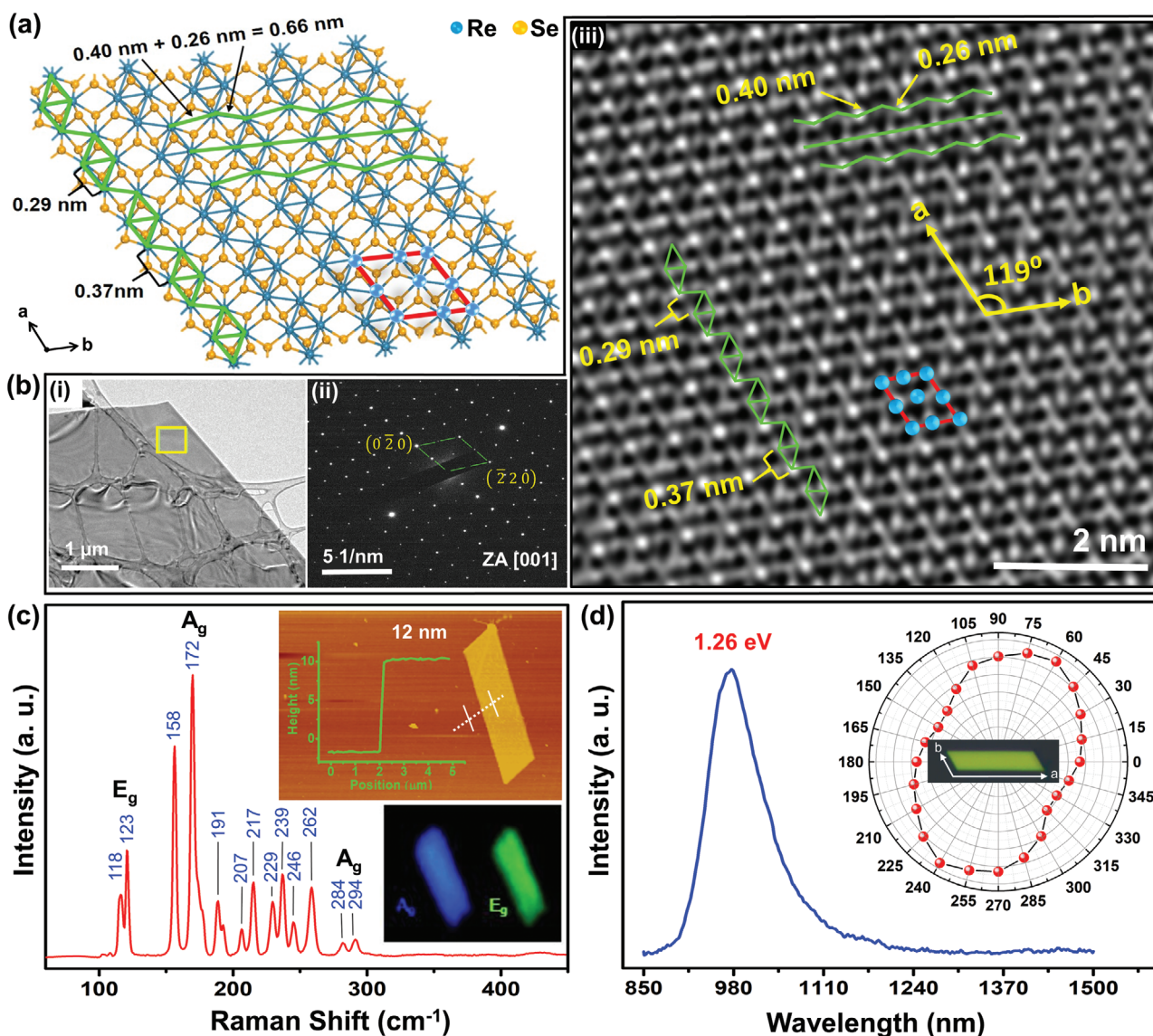
2. Results and Discussion

A top view of the $ReSe_2$ crystal structure is shown in **Figure 1**a, in which the Re atoms are surrounded by the Se atoms in a distorted octahedron and the Re–Re chains are formed with diamond-like clusters (as highlighted in green on the left edge) along the *a*-axis of the crystal.[36,37] The $ReSe_2$ crystal possesses a quasi-one-dimensional array with the unique Peierls distortion (i.e., the separations of 0.29 and 0.37 nm) along the *a*-axis (see the observation in Figure 1b(iii)).[38] In this study, $ReSe_2$ nanosheets were synthesized by atmospheric pressure chemical vapor deposition (APCVD) with the synthesis protocols given in Section S1 and Figure S1 (Supporting Information). In Figure 1b, the i) transmission electron microscopy (TEM) image, ii) selected-area electron diffraction (SAED) pattern along the [001] zone axis, and iii) high-resolution (HR)-TEM image of the APCVD-grown $ReSe_2$ nanosheets display the single-crystalline structure with an angle of 119° between the *a*- and *b*-axes and the lattice spacing of 0.66 nm along the *b*-axis.[39]

Figure 1c shows the Raman spectrum of the APCVD-grown 12 nm-thick $ReSe_2$ nanosheets (in the upper inset) involving 13 distinctive vibrational modes at 100–300 cm^{-1} and is identical to that of the pristine $ReSe_2$ crystal reported previously.[33,40] While the twisting and rocking of the Re atoms are responsible for the vibrational modes at <130 cm^{-1}, the stretching and wagging of the Se atoms are assigned to the higher frequency modes at >150 cm^{-1}.[40] Specifically, the Raman signals at ≈118/123 cm^{-1} are attributed to the in-plane vibration (E_g). The strong peaks at ≈158/172 cm^{-1} along with the relatively weak peaks at 284/294 cm^{-1} are caused by the out-of-plane vibration (A_g). It is also noted that the vibrational frequencies of the $ReSe_2$ nanosheets are considerably independent of their crystal thickness because of the decoupling of lattice vibrations among adjacent layers.[39,40] The Raman mapping images via the A_g (blue) and E_g (green) modes (in the lower inset of Figure 1c) further confirm structural homogeneity in the high-quality $ReSe_2$ nanosheets. The elemental compositions of the as-grown $ReSe_2$ nanosheets were determined to be Re:Se ≈ 1:2 by X-ray photoelectron spectroscopy (XPS, Figure S2 in Section S2, Supporting Information), and the uniform distribution of the Re and Se atoms over the entire crystal domain was further supported by the elemental mapping of energy dispersive spectroscopy (EDS) (Figure S3 in Section 2, Supporting Information).

In Figure 1d, the observed photoluminescence (PL) spectrum shows a bandgap of 1.26 eV (≈984 nm) for the ambipolar $ReSe_2$ nanosheets. The PL signal originates mainly from the dominant band-edge excitons of E_1^{ex} and E_2^{ex} with their excitonic dipole emissions perpendicular and parallel, respectively, to the *a*-axis of the $ReSe_2$ crystal as studied previously by cryogenic PL spectroscopy.[41] Based on its crystal symmetry, $ReSe_2$ inherits an anisotropic in-plane polarization arising from the optically biaxial nature.[37,42] In the inset of Figure 1d, the anisotropic nature of the as-grown $ReSe_2$ nanosheets is evidenced by the observed PL polarization with a maximal intensity at $\theta = 60°$ (with $\theta = 0°$ defined along the *a*-axis), resulting from the orthogonal polarizations of the dominant E_1^{ex} and E_2^{ex} excitons and some other weak excitonic emissions.[43]

Next, a $ReSe_2$-based LET device (as illustrated in **Figure 2**a) was fabricated with the *a*-axis of the $ReSe_2$ crystal aligned along the conducting channel (see details in Section S3, Supporting Information). An ultrathin HfO_2 layer (10 nm in thickness) of a high dielectric constant (*k*) was used to enhance the device capacitance and reduce the gate leakage current by suppressing
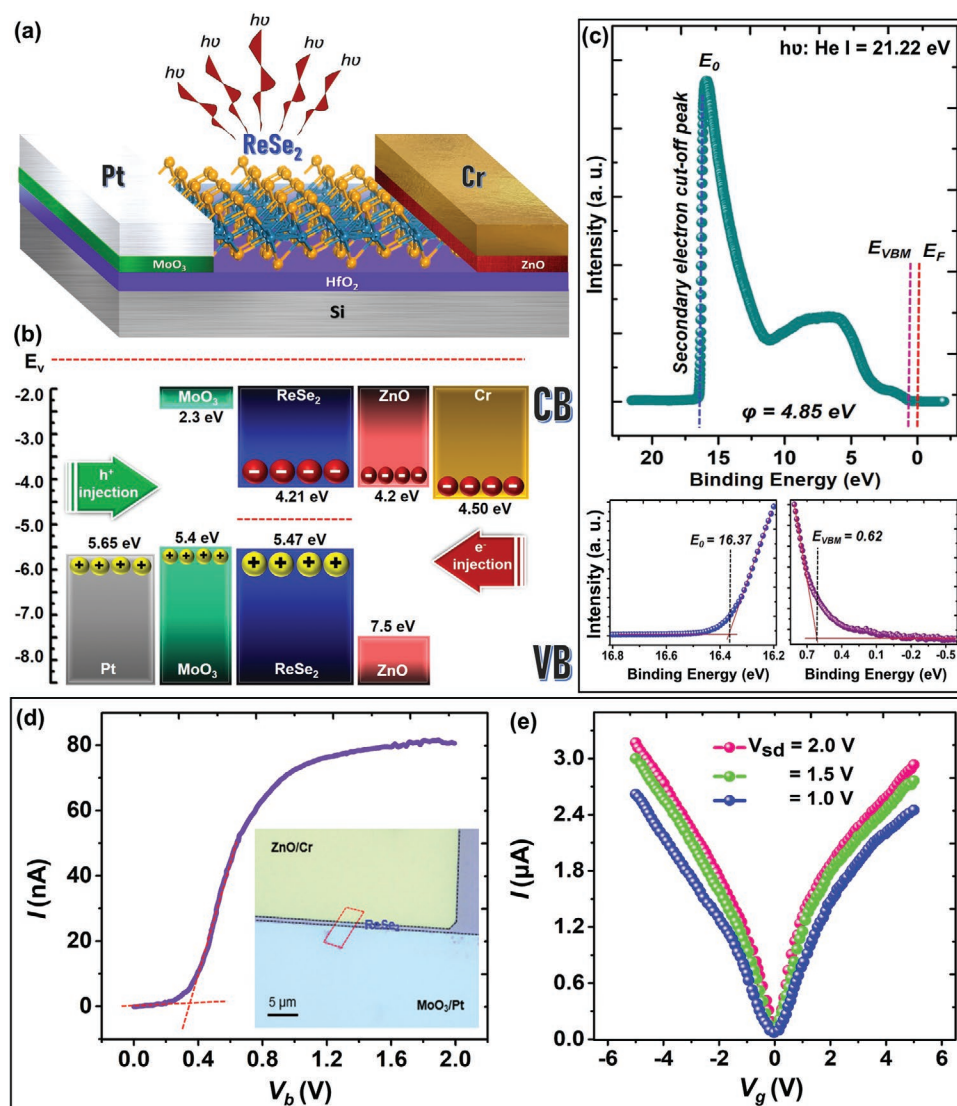
**ADVANCED
SCIENCE NEWS**

www.advancedsciencenews.com

**ADVANCED
OPTICAL
MATERIALS**

www.advopticalmat.de

Figure 1. a) An illustration of the $ReSe_2$ crystal displays the Re–Re chain of diamond-like clusters along the *a*-axis (highlighted by green on the left edge), in which different interatomic distances of 0.29 nm and 0.37 nm are due to the Peierls distortion. A red square encompassing nine blue-colored Re atoms (also demarcated by the same color in panel (b-iii)) represents a unit cell. b) The i) TEM image, ii) SAED pattern along the [001] axis, and iii) HR-TEM image (taken for the yellow-square region in panel (b-i)) of the APCVD-grown $ReSe_2$ nanosheets demonstrate the single-crystalline $ReSe_2$ structure. The HR-TEM image also reveals the Peierls lattice distortion (the separations of 0.29 nm and 0.37 nm) along the *a*-axis, the separations of 0.26 nm and 0.40 nm along the *b*-axis, and the intersection angle of 119° between the *a*- and *b*- axes. c) Raman spectrum of the as-grown $ReSe_2$ nanosheets was observed at 100–300 cm^{-1}. The upper inset shows the atomic force microscopy (AFM) topograph and thickness profile of the $ReSe_2$ nanosheets. The lower inset displays the Raman mapping images via the A_g (blue) and E_g (green) modes, validating structural homogeneity in the $ReSe_2$ nanosheets. d) PL spectrum of the 12 nm-thick $ReSe_2$ nanosheets, excited by a 532 nm laser with the polarization along the *a*-axis, indicates the bandgap energy of 1.26 eV (≈984 nm). In the inset, the polarized PL intensity of the anisotropic $ReSe_2$ crystal was measured at every 15° interval with $\theta = 0°$ defined along the *a*-axis of the $ReSe_2$ crystal.

direct tunneling.[44] In line with the energy alignment (Figure 2b), a pair of asymmetric Pt/Cr electrodes were selected because their work functions (Pt: 5.65 eV and Cr: 4.5 eV)[45] come close to the valence band maxima (VBM at 5.47 eV) and conduction band minima (CBM at 4.21 eV) of the $ReSe_2$ channel, respectively. These matches in energy at the metal–semiconductor interface reduce the Schottky barrier height (SBH), hence retaining the intrinsic transport in a $ReSe_2$-LET. The Fermi level of the as-grown $ReSe_2$ nanosheets, measured to

be 4.85 eV by ultraviolet photoelectron spectroscopy (UPS, see details in Figure 2c and Section S4, Supporting Information), falls nearly in the middle of the bandgap of the $ReSe_2$ crystal and agrees with the nature of an ambipolar crystal.

It is known that the FLP effect plays a crucial role in the metal-semiconductor interface,[46,47] where a large energy difference between the Fermi level of the semiconductor channel and the work functions of metal electrodes causes strong FLP with a high SBH in the electrical transport. As a strategy to

**ADVANCED
SCIENCE NEWS**

www.advancedsciencenews.com

**ADVANCED
OPTICAL
MATERIALS**

www.advopticalmat.de

Figure 2. a) A schematic illustration of an ambipolar ReSe$_2$-LET device fabricated with asymmetric Pt/Cr electrodes to emit NIR EL. b) An energy diagram displays the work functions of the contact electrodes of Pt and Cr are very close to the VBM and CBM of ReSe$_2$, respectively. These energy matches assist the injections of bipolar carriers from opposite electrodes to facilitate the electron-hole recombination in the ReSe$_2$ channel. c) The Fermi level of the as-grown ReSe$_2$ nanosheets was measured to be 4.85 eV by UPS. d) For the as-fabricated ReSe$_2$-LET device (with an optical image shown in the inset), the output curve measured at $V_g = 0$ V and e) the transfer curves scanned in the range of -5 V $< V_g < 5$ V at various V_b were investigated.

address this problem, we inserted a metal-oxide layer at the metal–semiconductor interface for Fermi-level depinning to reduce the SBH. As depicted in Figure 2a, 10 nm-thick MoO$_3$ and ZnO layers were introduced to the Pt/ReSe$_2$ and Cr/ReSe$_2$ interfaces, respectively, to facilitate the hole and electron injections.[48–51] Additionally in Figure 2b, the large energy differences between the CBMs of MoO$_3$ and ReSe$_2$[48] and between the VBMs of ZnO and ReSe$_2$[50] could block the electrons and holes, respectively, from drifting into the opposite electrodes. As a result, the accumulated bipolar carriers in the ReSe$_2$ channel enrich the electron-hole recombination rate for strong luminescence.

Electrical transport of the ambipolar ReSe$_2$-LET was measured with its output curve shown in Figure 2d, where the low turn-on voltage of 0.38 V is comparable to the previous

reports.[52,53] The output current increases with increasing V_b and becomes saturated at $V_b > 1.2$ V. The gate-dependent output characteristics (Figure S4, Supporting Information) and the current saturation at high bias voltages are discussed in Section S5 of the Supporting Information. Figure 2e shows the transfer curves of the ReSe$_2$-LET at various back-gate voltages (V_g) scanned from -5 to $+5$ V. The neutrality points of these symmetric transfer curves, measured at various V_b, are all located nearly at $V_g = 0$ V, reflecting this high-quality ambipolar device. The field-effect mobilities of $\mu_h = 0.299$ cm^2 V^{-1} s^{-1} for holes and $\mu_e = 0.264$ cm^2 V^{-1} s^{-1} for electrons at $V_b = 1$ V (Figure S5 in Section S6, Supporting Information) were determined for this ambipolar ReSe$_2$-LET. Additionally, we also tested the electrical transports of ReSe$_2$-LETs fabricated on a hexogonal boron nitride (h-BN)/SiO$_2$/Si substrate (Figure S6

in Section S7, Supporting Information). At high $V_b > 2$ V and $V_g > 25$ V, the field-effect mobilities of $\mu_h = 2.27$ cm^2 V^{-1} s^{-1} and $\mu_e = 1.21$ cm^2 V^{-1} s^{-1} could be achieved in the linear regimes and are comparable to, or higher than, the values of the CVD-grown ReSe$_2$ crystals reported earlier.[33,54–56] Since the ReSe$_2$-LET devices with an ultrathin HfO$_2$ dielectric layer (10 nm in thickness) exhibited superior electrical properties at low V_b and V_g (as displayed in Figure 2e, where prominent ambipolar characteristics of the symmetric bipolar electric tranports with the neutrality points nearly at $V_g = 0$ V are demonstrated), we used the ReSe$_2$-LET devices fabricated on HfO$_2$/Si substrates in the following experiments.

To probe the EL from a ReSe$_2$-LET device, a frequency-modulation detection system was employed (as illustrated in **Figure 3**a), where a lock-in amplifier was coupled with a liquid nitrogen-cooled germanium (Ge) detector sensitive to the NIR light at 800–1650 nm and controlled by the LabVIEW program (Figure S7 and Section S8, Supporting Information). The lock-in amplifier is a phase-sensitive detection system of applying an alternating current (AC) modulation-demodulation technique, which enables detecting small AC signals hidden in a noisy environment. The EL from ReSe$_2$-LET was detected with the LET device aligned to face the Ge detector, of which all measurements were performed inside a dark Faraday cage under ambient conditions. The electrically shielded Faraday cage was electrical grounding, resistant to electromagnetic interference, and maintained at a relative humidity of 10% to prevent the Ge detector's window from fogging.

To achieve the maximal EL output from the ReSe$_2$-LET device, we first adjusted the relative positions of the apparatus used in the experiments (Figure 3a) and found that the optimal separation between ReSe$_2$-LET and the Ge detector is 12.5 mm. With this geometric alignment, we further tested the device performance by varying i) the modulation frequency (f_m) of the lock-in amplifier, ii) the V_b applied to the ReSe$_2$-LET, and iii) the channel length (l_c) of the ReSe$_2$-LET, and monitoring iv) the stability of the EL from ReSe$_2$-LET.
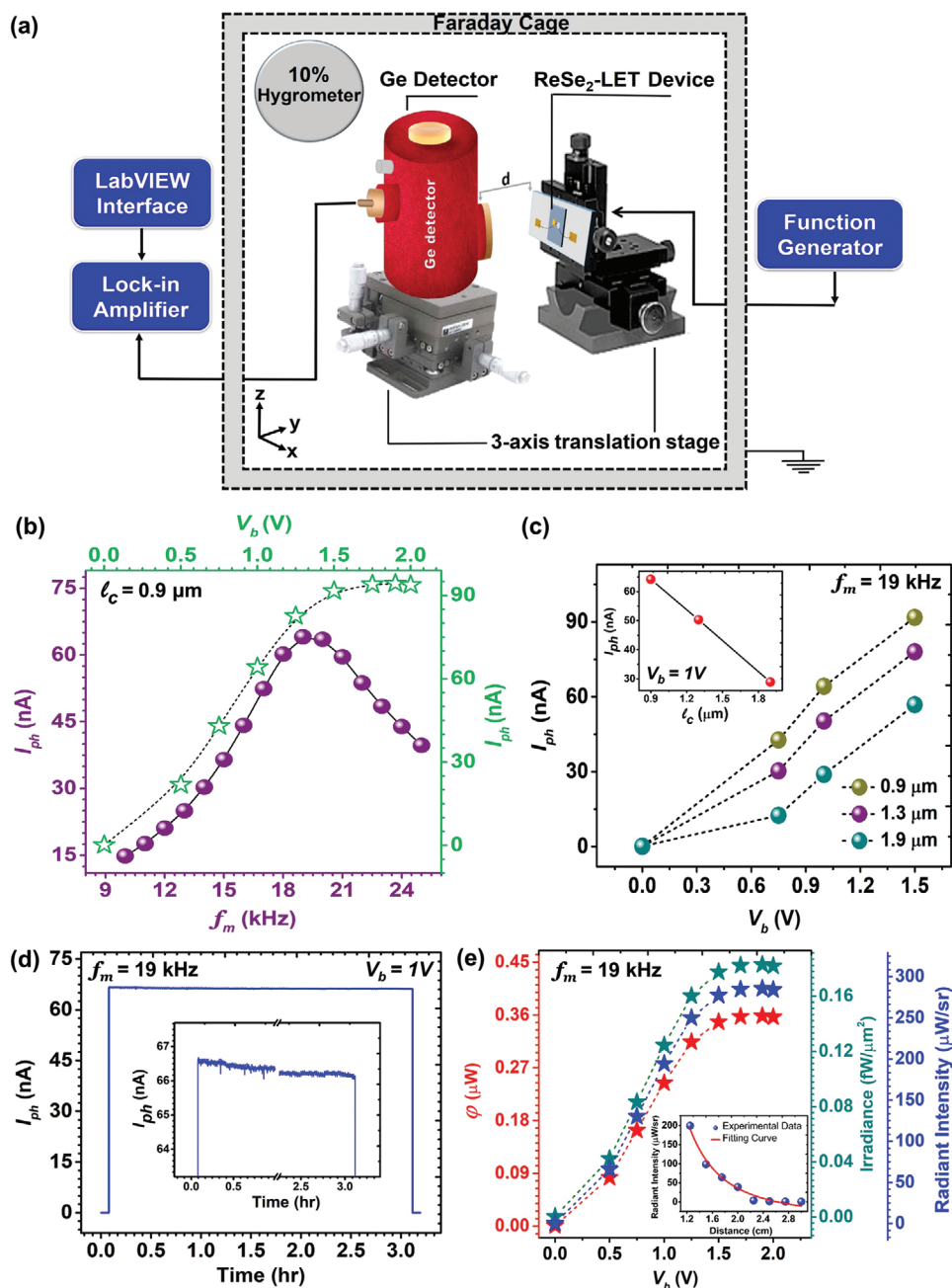
Figure 3b (the purple curve, left ordinate) shows that the photocurrent (represented by I_{ph} hereafter), excited by the EL from ReSe$_2$-LET at $V_b = 1$ V and detected by the Ge detector, can reach 65 nA when setting $f_m = 19$ kHz in the lock-in amplifier. The EL-exciting I_{ph} was further tested by varying V_b at 0–2 V with $f_m = 19$ kHz (see measurements in Figure S8 in Section S9, Supporting Information). Figure 3b (the green curve, right ordinate) summarizes the I_{ph} versus V_b plot (with the data points from Figure S9 in Section S10, Supporting Information), where the I_{ph} increases monotonically at low V_b and becomes saturated at $V_b > 1.5$ V. To confirm that the detected I_{ph} was excited genuinely by the EL from ReSe$_2$-LET, we conducted a control test with a device without the ReSe$_2$ conducting channel (i.e., a blank device has electrodes only). The red trace in Figure S9 (Supporting Information) shows a negligible I_{ph} response from this blank device even operating at $V_b = 0$–2 V, verifying that the I_{ph} was truly excited by the ReSe$_2$-LET-emitting EL, rather than the electrical interference due to a device–metal contact and/ or cross-talk between signaling pathways during the measurements. Moreover, while the radiative EL from the ReSe$_2$-LET devices is resulted from the intralayer electron-hole recombination, the interlayer recombination from the MoO$_3$/ReSe$_2$, or

ZnO/ReSe$_2$, interface can be neglected. The spatially indirect nature of interlayer excitons with the reduced overlap of the electron and hole wavefunctions results in smaller oscillation strength (and recombination rate) than that of the spatially direct intralayer excitons by orders of magnitude.[57,58,59]

When an LET device contains different l_c, the charge mobilities and recombination rate of bipolar carriers as well as the device's turn-on voltage may alter accordingly. As a result, the l_c of an LET device is crucial for its EL efficiency. In Figure 3c, the EL-exciting I_{ph} decreases as the l_c of ReSe$_2$-LET increases from 0.9 to 1.9 μm. Additionally in Figure 3d, the real-time measured EL emitted from the ReSe$_2$-LET ($l_c = 0.9$ μm, $V_b = 1$ V, and $f_m = 19$ kHz) was demonstrated stable, with the EL intensity variation within only ≈1% for at least 3 h' emission. Subsequently, the ReSe$_2$-LET devices of $l_c = 0.9$ μm operated at the experimental conditions of $V_b = 1$ V and $f_m = 19$ kHz were adopted in the following studies unless otherwise indicated.

The radiant power (Φ) of the ReSe$_2$-LET was calculated from the I_{ph} detected by the Ge detector using the equation $\Phi = \left[\dfrac{I_{ph}}{q_p e}\right]\dfrac{hc}{\lambda}$, where q_p is the quantum yield of the Ge detector, e is the elementary charge, h is the Plank's constant, c is the velocity of light, and λ is the wavelength of luminescence.[60] The quantum yield (q_p) of the Ge detector at 980 nm was determined from the detector's wavelength-dependent responsivity graph (Figure S11 and Section S12, Supporting Information). As shown in Figure 3e (the red curve, left ordinate), the radiant characteristics of the ReSe$_2$-LET resemble a typical LED, i.e., the radiant power increases gradually as the drive voltage escalates at 0 V $< V_b < 1.5$ V, reaches the maximal ≈0.35 μW at V_b ≈1.5 V and becomes saturated at even higher V_b. Assuming that all luminescence from the ReSe$_2$-LET fell on the active detection element (5 mm in diameter) of the Ge detector, the power conversion efficiency was estimated to be $\eta = 31.9\%$ (with the calculations given in Section S13 of the Supporting Information). Taking the solid angle of the emitting light from ReSe$_2$-LET into consideration, Figure 3e (the green curve, right ordinate) shows the calculated irradiance of the ReSe$_2$-LET. In the inset of Figure 3e, the I_{ph} intensity obeys an inverse square law, i.e., inversely proportional to the square of the distance from the ReSe$_2$-LET source.
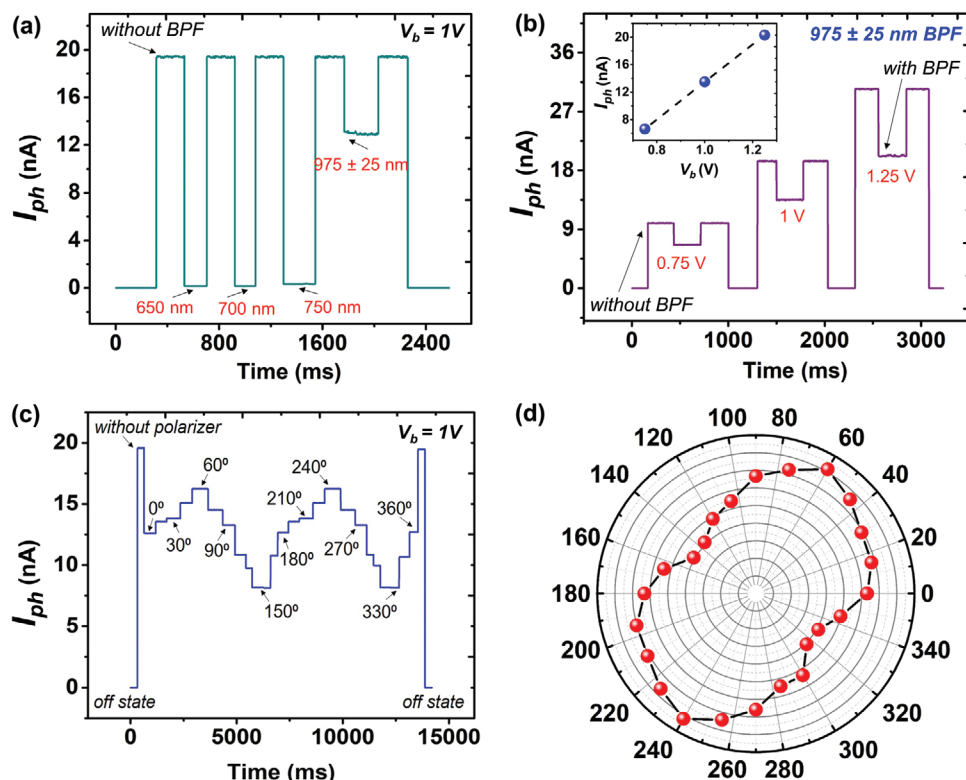
Because the EL intensity emitted from the ReSe$_2$-LET was too weak to be measured with an ordinary monochromator to identify its wavelength (λ), we applied a series of bandpass filters (BPFs) to determine the spectral region of the EL (see Section S8 and Figure S7 in Supporting Information). According to the bandgap energy of 1.26 eV ($\lambda \approx 984$ nm) revealed from the observed PL for the as-grown ReSe$_2$ nanosheets (Figure 1d), a set of BPFs with the center wavelength covering 650–750 nm (each has ±50 nm bandwidth) and 975 ± 25 nm (with ≈68% transmission at 984 nm) were inserted between the ReSe$_2$-LET device and the Ge detector to distinguish the EL wavelength. Shown in **Figure 4**a is the EL from ReSe$_2$-LET, attenuated completely by the BPFs with the center wavelengths at 650, 700, and 750 nm, but transmitted ≈68% when using the BPF of 975 ± 25 nm. To further confirm that the detected NIR EL is truly emitted from the ReSe$_2$-LET, we placed the BPF of 975 ± 25 nm in front of the Ge detector and applied various V_b to the LET device (Figure 4b). In the inset of Figure 4b, the I_{ph}

**ADVANCED
SCIENCE NEWS**

www.advancedsciencenews.com

**ADVANCED
OPTICAL
MATERIALS**

www.advopticalmat.de

Figure 3. a) To detect the EL from ReSe₂-LET, the experimental setups, including a ReSe₂-LET device, a Ge detector, and a lock-in amplifier, were placed inside a Faraday cage (represented by the grey box) maintained at a relative humidity of ≈10%. b) (the purple curve, left ordinate) The I_{ph} excited by the EL from ReSe₂-LET at $V_b = 1$ V was tested by varying the modulation frequency (f_m) of the lock-in amplifier to obtain the optimal $f_m = 19$ kHz. (the green curve, right ordinate) With f_m fixed at 19 kHz hereafter, the I_{ph} was measured by varying V_b at 0–2 V. c) The I_{ph} excited by the EL from ReSe₂-LETs with different l_c was investigated at $V_b = 0$–1.5 V. The inset shows that I_{ph} decreases as l_c increases from 0.9 to 1.9 μm. d) The stability of the I_{ph} intensity was tested in real-time measurement. A magnified scale, belonging to the parts of the early and late measurements, is shown in the inset. e) The EL presented by radiant power (the red curve, left ordinate), or converted to irradiance (the green curve, right ordinate) or radiant intensity (the blue curve, right ordinate), was investigated at $V_b = 0$–2 V. (inset) The distance-dependent radiant intensity from the ReSe₂-LET was measured at every 2.5 mm interval with a three-axis XYZ micropositioner stage (see measurements in Figure S10 and Section S11, Supporting Information).

intensity exhibits a quite linear response to different V_b from 0.75 to 1.25 V with the increasing trend in accordance with that measured in Figure 3b. This outcome validates that the EL was emitted indeed from the ReSe₂-LET with the wavelength within the NIR region of 975 ± 25 nm.

Finally, we investigated the room-temperature angle-dependent EL from the ReSe₂-LET (Figure 4c) with $\theta = 0°$ defined along the a-axis of the ReSe₂ crystal. The observed polarization-dependent EL plot (Figure 4d) exhibits a two-lobe-shaped EL pattern orienting at $\theta = 60°$, which is

**ADVANCED
SCIENCE NEWS**

www.advancedsciencenews.com

**ADVANCED
OPTICAL
MATERIALS**

www.advopticalmat.de

Figure 4. a) The wavelength of the EL emitted from the ReSe$_2$-LET was filtrated by a series of BPFs with the center wavelengths of 650, 700, and 750 nm (each has ±50 nm bandwidth), and 975 ± 25 nm (with ≈68% transmission at 984 nm). The EL from ReSe$_2$-LET was measured to transmit the BPF of 975 ± 25 nm by ≈68%. b) The I_{ph} excited by the EL from ReSe$_2$-LET operated at different V_b was compared with or without inserting the BPF (975 ± 25 nm) between the ReSe$_2$-LET and Ge detector. In presence of this BPF, the I_{ph} was observed to drop 32 ± 1% (consistent with the ≈68% transmission of this BPF), when the ReSe$_2$-LET was operated at V_b = 0.75, 1, and 1.25 V, respectively. The inset shows the I_{ph} in response to various V_b applied to the ReSe$_2$-LET device (with inserting the BPF). c) Polarization-dependent I_{ph}, excited by the EL from ReSe$_2$-LET, was measured at every 15° interval with $\theta = 0°$ defined along the a-axis of the ReSe$_2$ crystal. d) Summarizing the data points measured in (c), the polar plot shows that the maximal EL intensity occurred at $\theta = 60°$.

consistent with the polarized PL detected in Figure 1d, demonstrating the anisotropic in-plane polarization in the optically biaxial ReSe$_2$ crystal.

3. Conclusion

High-quality ReSe$_2$ nanosheets were synthesized with an APCVD method. The structural, spectroscopic, and topographic characterizations of the as-grown ReSe$_2$ nanosheets validate the superior anisotropic ambipolar ReSe$_2$ single crystal with the Fermi level lying nearly in the middle of its band gap. Asymmetric Pt/Cr electrodes were selected to fabricate an ambipolar ReSe$_2$-LET with the balanced number densities and field-effect mobilities of bipolar carriers, leading to a low turn-on voltage device. Room-temperature NIR EL emitted from the as-fabricated ReSe$_2$-LETs was observed unprecedentedly. The experimental parameters of f_m, V_b, and l_c implemented in the optoelectronic operations were optimized to achieve the maximal EL output from the ReSe$_2$-LET device. The stable NIR EL from ReSe$_2$-LET is polarization-dependent, manifesting the inherent anisotropic in-plane excitons of ReSe$_2$. This study demonstrates the highly stable NIR EL from ReSe$_2$-FETs, which can be further amplified with the assistance of an optical cavity

resonator to enhance the NIR EL intensity in the future study. This work proves the potential of 2D material-fabricated LETs as a promising pathway for ultrathin scalable data communication electronics. In the era of booming LiFi technology for ultrafast optical data transfer, the ambient temperature operating NIR LET devices with a low turn-on voltage can be in high demand for future optoelectronics.

4. Experimental Section

HR-TEM of the as-grown ReSe$_2$ nanosheets, transferred on a leicy-carbon-coated grid,[6] was conducted in a TEM (JEOL, JEM-2100F) with an operating voltage of 200 kV. The surface topography and height profiles of ReSe$_2$ nanosheets were measured by AFM (Bruker Dimension Icon). Raman spectra were acquired using a Raman spectrometer (NT-MDT, NTEGRA Spectra) equipped with an excitation laser at 633 nm and a monochromator with a grating of 1800 grooves mm^{-1}. The wavenumber measured in the Raman spectra was calibrated against the peak of Si at 520 cm^{-1}. The polarized PL from ReSe$_2$ nanosheets was acquired with a micro-Raman spectrometer (Horiba, LabRAM HR Evolution), including an optical microscope (Olympus, CX41), a monochromator with a grating of 950 grooves mm^{-1}, a detector (Jobin Won Horiba, SDrive-500 Syncerity), and a 532 nm laser. The polarized PL signals were measured at every 15° interval by rotating a linear polarizer. Topological elemental mapping of ReSe$_2$ nanosheets was conducted in a field-emission gun

2102580 (7 of 9)

scanning electron microscope (FEG-SEM) (Jeol, JSM-7800F) equipped with EDS. The XPS spectra were obtained using an ESCA spectrometer (VG Scientific, Escalab 250) with a monochromatic X-ray source (1486.6 eV Al Kα) and analyzed with Casa XPS software (v.2.3.17, Casa Software Ltd., Wilmslow, U.K.). The binding energies observed in the XPS were calibrated against the carbon C 1s peak at 284.8 eV prior to analysis and the Shirley–Sherwood method was employed to subtract the background. The Fermi level of ReSe$_2$ nanosheets was determined by UPS (ULVAC-PHI PHI 5000 VersaProbe II) using the He I excitation of 21.22 eV with an externally applied potential of 5 V to the sample. For the EL measurements, the ReSe$_2$-LET device was frequency modulated using the square wave generated from a function generator (Stanford Research Systems, DS335). The EL emitted from ReSe$_2$-LET was filtered by a BPF of 975 ± 25 nm (Edmund Optics) or a linear polarizer (Edmund optics) and detected by a Ge detector (Teledyne Judson, J16D-M204-R05M Nitrogen Cooled) sensitive to the NIR light at 800–1650 nm. The signals detected by the Ge detector were fed into a lock-in amplifier (Stanford Research Systems, SR830 DSP), where the instruments were interfaced and controlled with the LabVIEW program.

Supporting Information

Supporting Information is available from the Wiley Online Library or from the author.

Conflict of Interest

The authors declare no conflict of interest.

Data Availability Statement

Research data are not shared.

[1] F. Xia, H. Wang, D. Xiao, M. Dubey, *Nat. Photonics* **2014**, *8*, 899.
[2] J. Wang, I. Verzhbitskiy, G. Eda, *Adv. Mater* **2018**, *30*, 1802687.
[3] D. B. Farmer, G. M. Roksana, V. Perebeinos, Y. M. Lin, G. S. Tuievski, J. C. Tsang, P. Avouris, *Nano Lett.* **2009**, *9*, 388.
[4] E. C. Peters, E. J. H. Lee, M. Burghard, K. Kern, *Appl. Phy. Lett.* **2010**, *97*, 193102.
[5] M. C. Lemme, F. H. L. Koppens, A. L. Falk, M. S. Rudner, H. Park, L. S. Levitov, C. M. Marcus, *Nano Lett.* **2011**, *11*, 4134.
[6] C. Rost, S. Karg, W. Riess, M. A. Loi, M. Murgia, M. Muccini, *Appl. Phy. Lett.* **2004**, *85*, 1613.
[7] R. S. Sundaram, M. Engel, A. Lombardo, R. Krupke, A. C. Ferrari, P. Avouris, M. Steiner, *Nano Lett.* **2013**, *13*, 1416.
[8] J. Zaumseil, H. Sirringhaus, *Chem. Rev.* **2007**, *107*, 1296.
[9] M. Muccinni, *Nat. Mater.* **2006**, *5*, 605.
[10] C. H. Lee, G. H. Lee, A. M. Van Der Zande, W. Chen, Y. Li, M. Han, X. Cui, G. Arefe, C. Nuckolls, T. F. Heinz, J. Guo, J. Hone, P. Kim, *Nat. Nanotech.* **2014**, *9*, 676.
[11] M. M. Furchi, A. Pospischil, F. Libisch, J. Burgdörfer, T. Mueller, *Nano Lett.* **2014**, *14*, 4785.
[12] M. Ahles, A. Hepp, R. Schmechel, H. Von Seggern, *Appl. Phy. Lett.* **2004**, *84*, 428.
[13] A. Risteska, D. Knipp, in *Handbook of Visual Display Technology* (Eds: J. Chen, W. Cranton, M. Fihn), Springer, Cham **2016**.
[14] A. Hepp, H. Heil, W. Weise, M. Ahles, R. Schmechel, H. von Seggern, *Phys. Rev. Lett.* **2003**, *91*, 157406.
[15] H. Kajii, T. Taneda, Y. Ohmori, *Thin Solid Films* **2003**, 334.
[16] M. A. Bader, G. Marowsky, A. Bahtiar, K. Koynov, C. Bubeck, H. Tillmann, H.-H. Hö, S. Pereira, *J. Opt. Soc. Am. B* **2002**, *19*, 2250.
[17] N. Tessler, D. J. Pinner, V. Cleave, P. K. H. Ho, R. H. Friend, G. Yahioglu, P. Le Barny, J. Gray, M. De Souza, G. Rumbles, *Synth. Met.* **2000**, *115*, 57.
[18] J. Zaumseil, *Adv. Func. Mater.* **2020**, *30*, 1905269.
[19] L. L. Chua, J. Zaumseil, J. F. Chang, E. C. W. Ou, P. K. H. Ho, H. Sirringhaus, R. H. Friend, *Nature* **2005**, *434*, 194.
[20] J. Zaumseil, R. H. Friend, H. Sirringhaus, *Nat. Mater.* **2006**, *5*, 69.
[21] J. Zaumseil, C. L. Donley, J. S. Kim, R. H. Friend, H. Sirringhaus, *Adv. Mater.* **2006**, *18*, 2708.
[22] T. Takenobu, S. Z. Bisri, T. Takahashi, M. Yahiro, C. Adachi, Y. Iwasa, *Phys. Rev. Lett.* **2008**, *100*, 066601.
[23] T. Takahashi, T. Takenobu, J. Takeya, Y. Iwasa, *Appl. Phys. Lett.* **2006**, *88*, 033505.
[24] T. Takahashi, T. Takenobu, J. Takeya, Y. Iwasa, *Adv. Func. Mater.* **2007**, *17*, 1623.
[25] S. Jo, N. Ubrig, H. Berger, A. B. Kuzmenko, A. F. Morpurgo, *Nano Lett.* **2014**, *14*, 2019.
[26] Y. J. Zhang, T. Oka, R. Suzuki, J. T. Ye, Y. Iwasa, *Science* **2014**, *344*, 725.
[27] M. Onga, Y. Zhang, R. Suzuki, Y. Iwasa, *Appl. Phys. Lett.* **2016**, *108*, 073107.
[28] I. Gutiérrez-Lezama, B. A. Reddy, N. Ubrig, A. F. Morpurgo, *2D Mater.* **2016**, *3*, 045016.
[29] K. Han, G. H. Ahn, J. Cho, D. H. Lien, M. Amani, S. B. Desai, G. Zhang, H. Kim, N. Gupta, A. Javey, *Appl. Phys. Lett.* **2019**, *115*, 011103.
[30] D. H. Lien, M. Amani, S. B. Desai, G. H. Ahn, K. Han, J. H. He, J. W. Ager, M. C. Wu, A. Javey, *Nat. Commun.* **2018**, *9*, 1229.
[31] N. W. Alcock, A. Kjekshus, A. Kjekshus, S. Gronowitz, R. A. Hoffman, A. Westerdahl, *Acta Chem. Scand.* **1965**, *19*, 79.
[32] B. Jariwala, D. Voiry, A. Jindal, B. A. Chalke, R. Bapat, A. Thamizhavel, M. Chhowalla, M. Deshmukh, A. Bhattacharya, *Chem. Mater.* **2016**, *28*, 3352.
[33] B. Kang, Y. Kim, J. H. Cho, *2D Mater.* **2017**, *4*, 025014.
[34] C. Zhou, Y. Zhao, S. Raju, Y. Wang, Z. Lin, M. Chan, Y. Chai, *Adv. Func. Mater.* **2016**, *26*, 4223.
[35] S. Yang, S. Tongay, Y. Li, Q. Yue, J. B. Xia, S. S. Li, J. Li, S. H. Wei, *Nanoscale* **2014**, *6*, 7226.

[36] A. Arora, J. Noky, M. Drüppel, B. Jariwala, T. Deilmann, R. Schneider, R. Schmidt, O. Del Pozo-Zamudio, T. Stiehm, A. Bhattacharya, P. Krüger, S. Michaelis de Vasconcellos, M. Rohlfing, R. Bratschitsch, *Nano Lett.* **2017**, *17*, 3202.

[37] H. J. Lamfers, A. Meetsma, G. A. Wiegers, J. L. De Boer, *J. Alloys Compd.* **1996**, *241*, 34.

[38] M. Kertesz, R. Hoffmann, *J. Am. Chem. Soc.* **1984**, *106*, 3453.

[39] H. Zhao, J. Wu, H. Zhong, Q. Guo, X. Wang, F. Xia, L. Yang, P. Tan, H. Wang, *Nano Res.* **2015**, *8*, 3651.

[40] D. Wolverson, S. Crampin, A. S. Kazemi, A. Ilie, S. J. Bending, *ACS Nano* **2014**, *8*, 11154.

[41] C. Ho, Z. Liu, *Nano Energy* **2019**, *56*, 641.

[42] C. H. Ho, M. H. Hsieh, C. C. Wu, Y. S. Huang, K. K. Tiong, *J. Alloys Compd.* **2007**, *442*, 245.

[43] C. H. Ho, Z. Z. Liu, M. H. Lin, *Nanotechnology* **2017**, *28*, 235203.

[44] J. Robertson, *EPJ Appl. Phys.* **2004**, *28*, 265.

[45] H. B. Michaelson, *J. Appl. Phys.* **1977**, *48*, 4729.

[46] Y. Zhao, K. Xu, F. Pan, C. Zhou, F. Zhou, Y. Chai, *Adv. Func. Mater* **2017**, *27*, 1603484.

[47] S. McDonnell, A. Azcatl, R. Addou, C. Gong, C. Battaglia, S. Chuang, K. Cho, A. Javey, R. M. Wallace, *ACS Nano* **2014**, *8*, 6265.

[48] K. J. Reynolds, J. A. Barker, N. C. Greenham, R. H. Friend, G. L. Frey, *J. Appl. Phys.* **2002**, *92*, 7556.

[49] H. You, Y. Dai, Z. Zhang, D. Ma, *J. Appl. Phys.* **2007**, *101*, 2005.

[50] A. K. K. Kyaw, X. W. Sun, C. Y. Jiang, G. Q. Lo, D. W. Zhao, D. L. Kwong, *Appl. Phys. Lett.* **2008**, *93*, 221107.

[51] W. J. E. Beek, M. M. Wienk, R. A. J. Janssen, *J. Mater. Chem.* **2005**, *15*, 2985.

[52] J. S. Ross, P. Klement, A. M. Jones, N. J. Ghimire, J. Yan, D. G. Mandrus, T. Taniguchi, K. Watanabe, K. Kitamura, W. Yao, D. H. Cobden, X. Xu, *Nat. Nanotech.* **2014**, *9*, 268.

[53] A. Pospischil, M. M. Furchi, T. Mueller, *Nat. Nanotech.* **2014**, *9*, 257.

[54] S. Jiang, Z. Zhang, N. Zhang, Y. Huan, Y. Gong, M. Sun, J. Shi, C. Xie, P. Yang, Q. Fang, H. Li, L. Tong, D. Xie, L. Gu, P. Liu, Y. Zhang, *Nano Res.* **2018**, *11*, 1787.

[55] F. Cui, X. Li, Q. Feng, J. Yin, L. Zhou, D. Liu, K. Liu, X. He, X. Liang, S. Liu, Z. Lei, Z. Liu, H. Peng, J. Zhang, J. Kong, H. Xu, *Nano Res.* **2017**, *10*, 2732.

[56] M. Hafeez, L. Gan, H. Li, Y. Ma, T. Zhai, *Adv. Mater.* **2016**, 8296.

[57] Y. Jiang, S. Chen, W. Zheng, B. Zheng, A. Pan, *Light Sci. Appl.* **2021**, *10*, 72.

[58] S. Ovesen, S. Brem, C. Linderälv, M. Kuisma, T. Korn, P. Erhart, M. Selig, E. Malic, *Commun. Phys.* **2019**, *2*, 23.

[59] P. Rivera1, J. R. Schaibley, A. M. Jones, J. S. Ross, S. Wu, G. Aivazian, P. Klement, K. Seyler, G. Clark, N. J. Ghimire, J. Yan, D. G. Mandrus, W. Yao, X. Xu, *Nat. Commun.* **2015**, *6*, 6242.

[60] C. Manilerd, *International Physics Olympiads: Problems and Solutions from 1967–1995*, Rangsit University Press, **1995**.

[61] R. J. Mathew, C. R. P. Inbaraj, R. Sankar, S. M. Hudie, R. D. Nikam, C.-A. Tseng, C.-H. Lee, Y.-T. Chen, *J. Mater. Chem. C* **2019**, *7*, 10996.

Supporting Information

Near-Infrared Electroluminescent Light-Emitting Transistors Based on CVD-Synthesized Ambipolar ReSe$_2$ Nanosheets

Roshan Jesus Mathew, Kai-Hsiang Cheng, Ching-Hong Hsu, Pradyumna Kumar Chand, Christy Roshini Paul Inbaraj, Yu-Lou Peng, Jung-Yen Yang, Chih-Hao Lee, and Yit-Tsong Chen*

R. J. Mathew, K.-H. Cheng, Prof. Y.-T. Chen
Institute of Atomic and Molecular Sciences, Academia Sinica, Taipei 10617, Taiwan.
Email: ytcchem@ntu.edu.tw

R. J. Mathew
Nano-Science and Technology Program, Taiwan International Graduate Program, Academia Sinica, Taipei, 11529, Taiwan.

K.-H. Cheng, C.-H. Hsu, P. K. Chand, Y.-L. Peng, Prof. Y.-T. Chen,
Department of Chemistry, National Taiwan University, Taipei 10617, Taiwan.

C. R. P. Inbaraj
Department of Physics, National Taiwan University, Taipei 10617, Taiwan

J.-Y. Yang
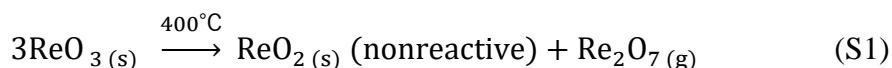National Applied Research Laboratories, Taiwan Semiconductor Research Institute, Hsinchu, 30078, Taiwan

R. J. Mathew, Prof. C.-H. Lee
Department of Engineering and System Science, National Tsing-Hua University, Hsinchu 30013, Taiwan.
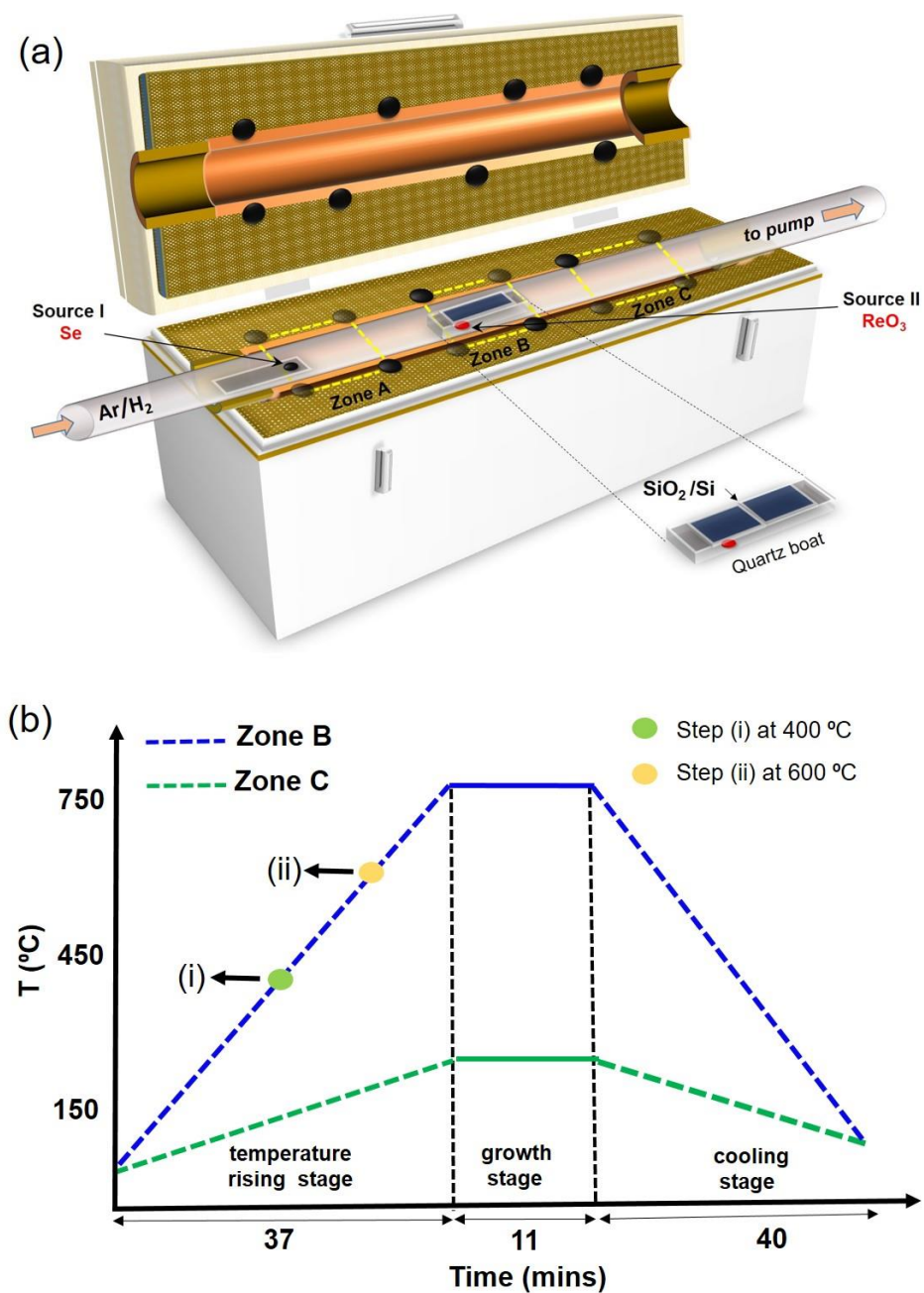
S1. APCVD Synthesis of Single-Crystalline ReSe$_2$ Nanosheets

As illustrated schematically in **Figure S1a**, an APCVD system was employed to grow single-crystalline ReSe$_2$ nanosheets. The APCVD system includes a three-zone tube furnace (Thermcraft Inc., Winston N.C, USA) with a quartz tube of 1" in diameter as a reaction chamber. Prior to APCVD reactions, a few diced silicon (Si) wafers of 1.5×2 cm^2 in size (with a 300 nm-thick SiO$_2$ dielectric layer), to be used as the growth substrates, were washed sequentially with acetone and isopropanol. In the APCVD synthesis of ReSe$_2$ nanosheets, rhenium oxide (ReO$_3$, with the melting point of 400 °C) powder and selenium (Se) pellets were used as chemical precursors for the sources of Re and Se. A custom-made quartz boat containing ReO$_3$ powder was covered by the pre-cleaned Si wafers and loaded to the center of the furnace (Zone B in **Figure S1a**). Comparatively, the Se pellets (with the melting point of 220 °C) were placed upstream near the furnace entrance and separated from the ReO$_3$ precursor by 17 cm. The temporal temperature profiles for the APCVD reactions are plotted in **Figure S1b**. During the APCVD reactions, while the temperature at Zone B was kept at 760°C, the Se precursor was maintained in a melting form until the temperature ramping approached the synthesis temperature. At 400 °C, ReO$_3$ was decomposed to the gaseous Re$_2$O$_7$ intermediate, which then reacted with Se vapor to form the ReSe$_2$ nucleation sites on the SiO$_2$/Si substrate to grow single-crystalline ReSe$_2$ nanosheets. The chemical reactions for the formation of ReSe$_2$ nanosheets involve

$$3\text{ReO}_{3\,(s)} \xrightarrow{400°C} \text{ReO}_{2\,(s)} \text{ (nonreactive)} + \text{Re}_2\text{O}_{7\,(g)} \qquad \text{(S1)}$$

$$\text{Re}_2\text{O}_{7\,(g)} + \text{Se}_{(g)} \xrightarrow{600°C} \text{ReSe}_{2\,(s)} \qquad \text{(S2)}$$
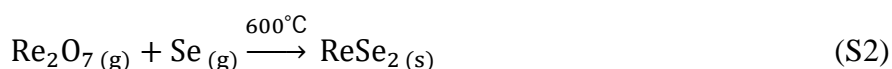
The growth time for the ReSe$_2$ nanosheets was lasted for 11 min in an ambient pressure with an Ar flow of 30 sccm. After reactions, the APCVD system was cooled down naturally.

Figure S1. (a) A schematic illustration of the APCVD setup used for the synthesis of single-crystalline ReSe$_2$ nanosheets. (b) The temporal temperature profiles of the APCVD reactions were adopted to grow ReSe$_2$ nanosheets.
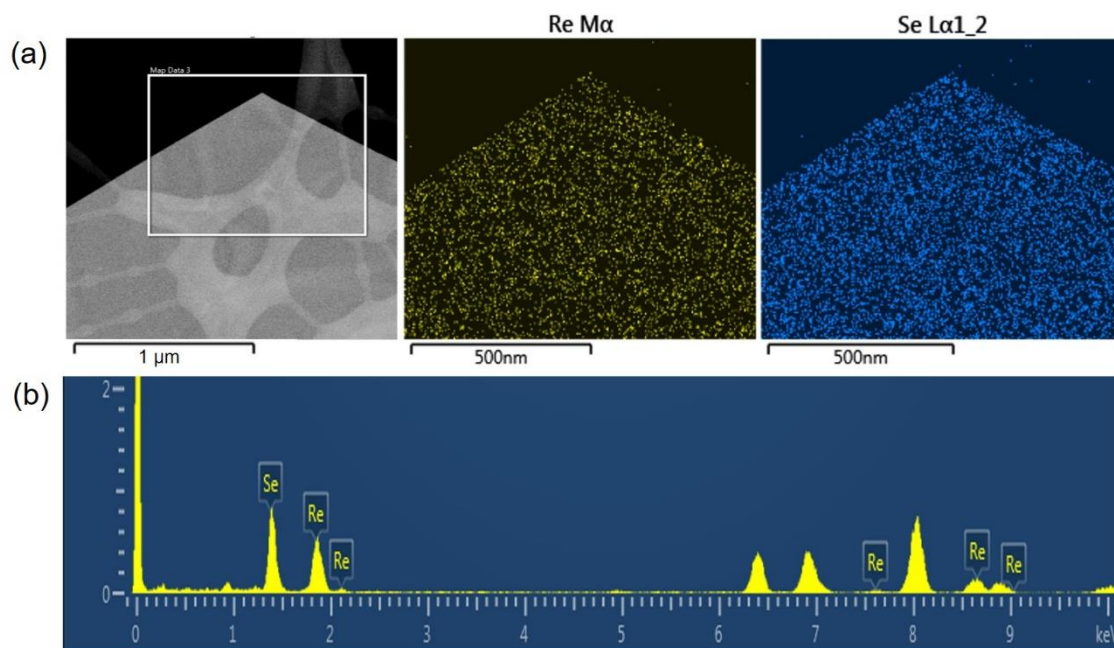
S2. Analysis of Elemental Compositions

The core-level elemental analysis for the as-grown ReSe$_2$ nanosheets was characterized by X-ray photoelectron spectroscopy (XPS) as shown in **Figure S2.** The observed doublets of Re 4f$_{7/2}$ and Re 4f$_{5/2}$ at 42.18 and 44.58 eV, respectively, were due to the spin-orbit coupling with the splitting of ~2.4 eV. However, relative to a standard Re metal, a blue-shift by 1.68 eV in these doublets was observed and is attributed to the bonding of Se–Re in ReSe$_2$. On the other hand, the Se 3d$_{5/2}$ and Se 3d$_{3/2}$ signals of the Se atom were deconvoluted to appear at 55.45 and 56.25 eV, respectively. **Figure S3** shows the elemental mappings of the Re and Se atoms, respectively, in the as-grown ReSe$_2$ nanosheets by energy dispersive spectroscopy (EDS). An analysis for the peak intensities gives a composition ratio of Re:Se = 1:1.97.
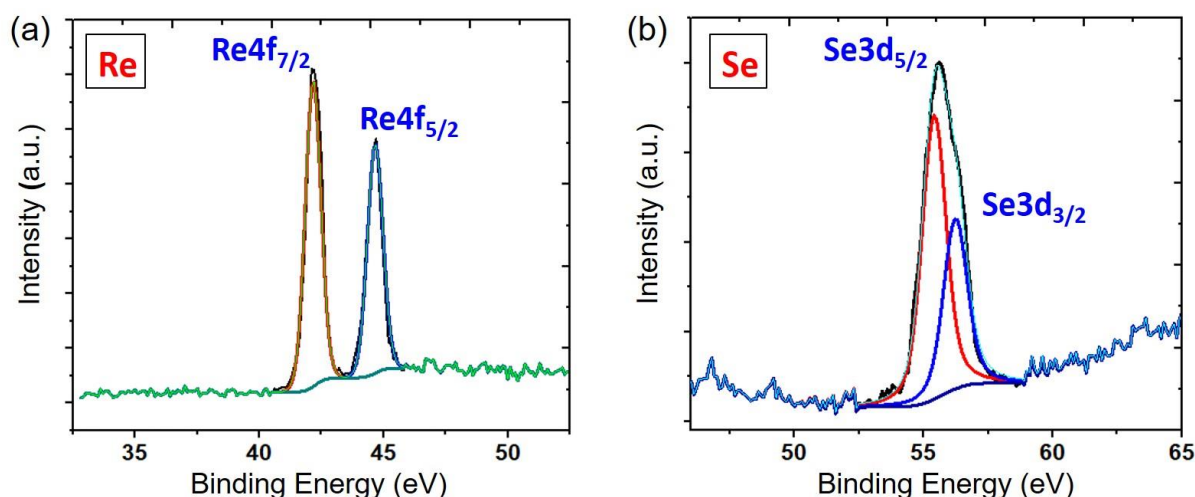
Figure S2. The XPS spectra of the as-grown ReSe$_2$ nanosheets show the doublets caused by the spin-orbit couplings in (a) Re atom (4f$_{7/2}$ at 42.18 eV and 4f$_{5/2}$ at 44.58 eV) and (b) Se atom (3d$_{5/2}$ eV at 55.45 and 3d$_{3/2}$ at 56.25 eV).

Figure S3. (a) The EDS elemental mappings (40 × 40 μm^2) of the as-grown ReSe$_2$ nanosheets dispaly the homogeneous distributions of the Re and Se atoms in the crystal domains. (b) An intensity analysis for the observed EDS spectrum reveals a composition ratio of Re:Se = 1:1.97 in the ReSe$_2$ nanosheets.

S3. Sample Transfer and Device Fabrication

ReSe$_2$ nanosheets on h-BN/SiO$_2$/Si substrates

The ReSe$_2$ nanosheets grown on Si wafers in the APCVD reactions were transferred to hexagonal boron nitride (h-BN)/SiO$_2$/Si substrates with a polymer-assisted dry transfer method. First, a large-area h-BN film was exfoliated with a PDMS stamp and then transferred to a Si wafer (denoted by h-BN/SiO$_2$/Si). Second, the as-grown ReSe$_2$ nanosheets were transferred with another PDMS stamp and adjusted precisely to locate on the h-BN/SiO$_2$/Si substrate with the assistance of a three-axis XYZ micropositioner stage.

ReSe$_2$ nanosheets on HfO$_2$/Si substrates

In addition, the ReSe$_2$ nanosheets grown on Si wafers in the APCVD reactions were also transferred to HfO$_2$/Si substrates by a polymer-assisted wet transfer method. First, poly(vinyl alcohol) (PVA) was spin-coated (3000 rpm for 120 sec) on top of an SiO$_2$/Si substrate containing the as-grown ReSe$_2$ nanosheets and then dried on a hot plate at 100 ^{o}C for 60 sec. Subsequently, the PVA/ReSe$_2$/SiO$_2$/Si was further spin-coated with PMMA (4000 rpm for 60 sec) and baked at 135 ^{o}C for 5 min to form PMMA/PVA/ReSe$_2$/SiO$_2$/Si. Thereafter, the PMMA/PVA/ReSe$_2$/SiO$_2$/Si was floated in 2M KOH solution to etch the SiO$_2$ layer. After delaminating from the SiO$_2$/Si substrate, the floating PMMA/PVA/ReSe$_2$ stack was scooped up onto a glass slide and washed thoroughly in cold water, followed by bailing it up onto an HfO$_2$/Si substrate (to form PMMA/PVA/ReSe$_2$/HfO$_2$/Si) and vacuum drying overnight. Finally, the PMMA/PVA layers were washed off from the ReSe$_2$/HfO$_2$/Si surface by dipping the PMMA/PVA/ReSe$_2$/HfO$_2$/Si in hot water, yielding a polymer-free ReSe$_2$/HfO$_2$/Si sample. The as-prepared ReSe$_2$/HfO$_2$/Si samples were kept in vacuum for further characterization and device fabrication.

The ReSe$_2$-LET devices were fabricated with a standard photolithography technique. In the first step, one side of the ReSe$_2$ channel was deposited with 10 nm-thick molybdenum

trioxide (MoO_3) by thermal evaporation, followed by sputter coating a 10 nm-thick platinum (Pt) electrode. In the second step, the other side of the $ReSe_2$ channel was deposited first with 10 nm-thick zinc oxide (ZnO) by sputter coating and then with a 20 nm-thick chromium (Cr) electrode by thermal evaporation. The Cr electrode was further encapsulated with a 25 nm-thick gold (Au) layer to prevent the electrode degradation from atmospheric exposure. The electrical transports of the as-fabricated $ReSe_2$-LET devices were measured at room temperature in a probe station (Lakeshore, TTPX) at 10^{-3} Torr equipped with a source meter (Keithley, 2636A).

S4. Ultraviolet Photoelectron Spectroscopy

The Fermi level and valence band maximum (VBM) of the ReSe$_2$ nanosheets were determined by ultraviolet photoelectron spectroscopy (UPS) with the He I radiation excitation at 21.22 eV. The onset and cutoff values in the observed UPS spectra (**Figure 2c** of the main text) were resolved with a standard procedure.[S1] The Fermi level/work function (ϕ) was calculated by

$$\phi = h\nu - E_0 \tag{S3}$$

where $h\nu$ is the photon energy of the radiation at 21.22 eV and E_0 is the binding energy of the ejected electron from the ReSe$_2$ nanosheets observed at 16.37 eV. Inserting these values into Eq. (S3), the resultant Fermi level/work function (ϕ) is

$$\phi = 21.22 - 16.37 = 4.85 \text{ eV} \tag{S4}$$

By subtracting the binding energy of the valence band maxima (E_{VBM}) located at 0.62 eV from the energy bang gap of 1.26 eV (determined from the PL spectrum shown in **Figure 1d** of the main text), the binding energy of the conduction band minima (E_{CBM}) was obtained at 0.64 eV. These values show the Fermi level is nearly centered between the VBM (at 5.47 eV from the main text) and CBM (at 4.21 eV from the main text), suggesting the nearly perfect ambipolar characteristic of the CVD-grown ReSe$_2$ nanosheets.

S5. Gate-dependent Output Characteristics of ReSe$_2$-LETs

The gate-dependent output curves of an ReSe$_2$-LET device (l_c = 900 nm) fabricated on HfO$_2$ (10 nm in thickness) gate dielectric exhibit non-linear characteristics at higher (back)gate (V_g) and bias (V_b) voltages **(Figure S4a)**. In contrast, linear output curves of a similar ReSe$_2$-LET device (l_c = 900 nm) on SiO$_2$ (50 nm in thickness) gate dielectric were observed at higher gate and bias voltages (**Figure S4b**). The non-linear output characteristics were observed only for the devices on HfO$_2$ dielectric at higher gate and bias voltages (resulting in the saturation of high carrier concentrations), which can be mainly attributed to the high-k dielectric-induced surface-optical phonon scattering in the devices. It has been studied that the high-k gate dielectrics, such as HfO$_2$ and Al$_2$O$_3$, in 2D materials-fabricated FET devices[S2–S7] can effectively reduce the Coulombic impurity scattering to increase the charge-carrier mobility in the conducting channel. In addition, the highly-polar high-k dielectrics can be polarized more easily in response to an external electric field, where the large polarization from the oscillating metal-oxide bonds in the dielectric layer couples strongly to the free carriers of the conducting channel.[S3, S6, S7] Hence, at higher drive voltages, the remote interaction between the charge carriers and the surface-optical phonons of the dielectric layer creates inelastic scattering, thereby limiting the charge transport in the conducting channel in close proximity with high-κ dielectrics.[S8, S9, S10] On that account, the ReSe$_2$-LETs fabricated on HfO$_2$ gate dielectric possess non-linear output characteristics at higher drive voltages.

On the other hand, the non-linear behavior at low V_b, irrespective of dielectric materials, is the characteristic property of *p-n* junction light-emitting devices.[S9] In this study, the ReSe$_2$-LETs fabricated on HfO$_2$ gate dielectric were chosen because the higher output current and carrier mobility of the ReSe$_2$-LETs can be achieved at relatively lower bias voltage.
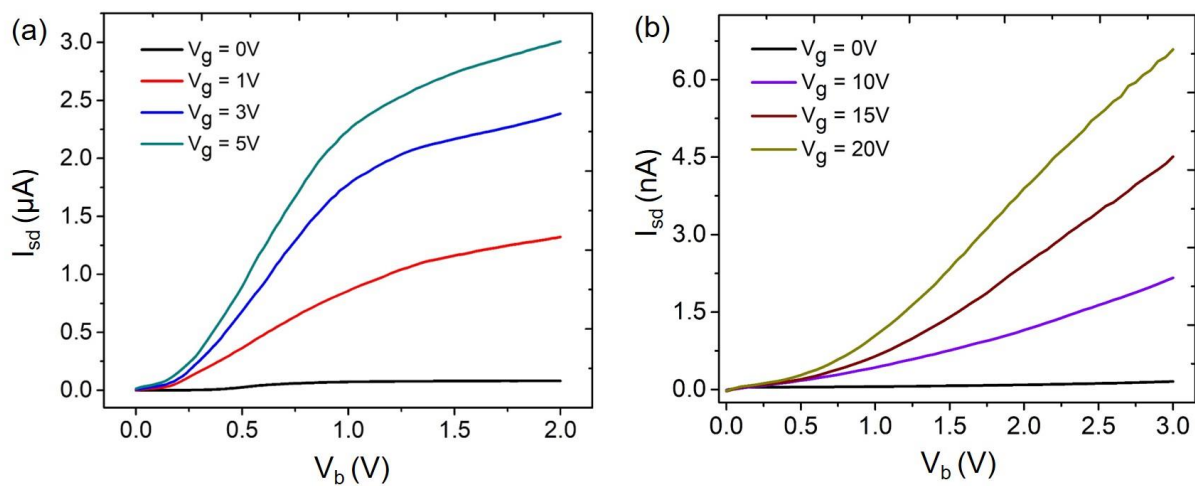
Figure S4. The gate-dependent output curves of the ReSe$_2$-LET devices ($l_c = 900$ nm) fabricated on (a) 10 nm-thick HfO$_2$ and (b) 50 nm-thick SiO$_2$ dielectric substrates.

S6. Field-Effect Mobilities of Bipolar Carriers in an ReSe₂-LET

From the recorded electrical transfer curves, the total resistance (R_{total}), which is composed of the contact resistance ($R_{contact}$) of electrode/ReSe₂ and the ReSe₂ channel resistance ($R_{channel}$), can be determined. The total resistance (R_{total}) of an ReSe₂-LET can be represented as a function of V_g[S11]

$$R_{total} = \frac{V_b}{I_{sd}} = R_{contact} + R_{channel}$$

$$= R_{contact} + \frac{L}{W} \frac{1}{\mu \cdot n(V_g - V_{cn})}$$

$$= R_{contact} + \frac{L}{W} \frac{1}{\mu \cdot \sqrt{n_0^2 + (C_g|V_g - V_{cn}|)^2}}$$

where L and W are the channel length and width, respectively, μ is the carrier mobility, n_o is the residual charge density at the charge neutrality point, C_g is the capacitance per unit area of the gate dielectric, and V_{cn} refers to the recorded potential shift from the charge neutrality point. By fitting the data points of the measured transfer curve to this formula, the carrier mobilities for both n-branch and the p-branch of the transfer curve can be obtained.
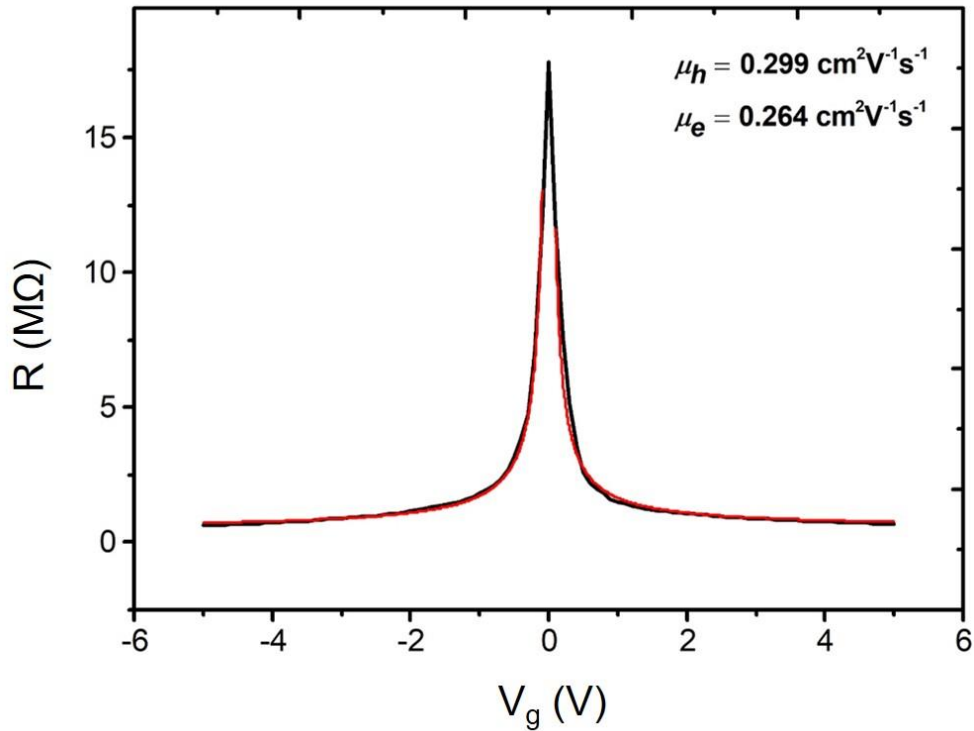
Figure S5. The field-effect mobilities of electrons ($\mu_e = 0.264$ cm^2/Vs) and holes ($\mu_h = 0.299$ cm^2/Vs) in an ReSe₂-LET were extracted from the measured gate-dependent resisrance curve, where a self-consistent diffusive transport model (red solid line) was applied to fit the experimental data (black solid line).

**S7. Electrical Characteristics of the ReSe₂-LET Fabricated on an h-BN/SiO₂/Si Substrate**
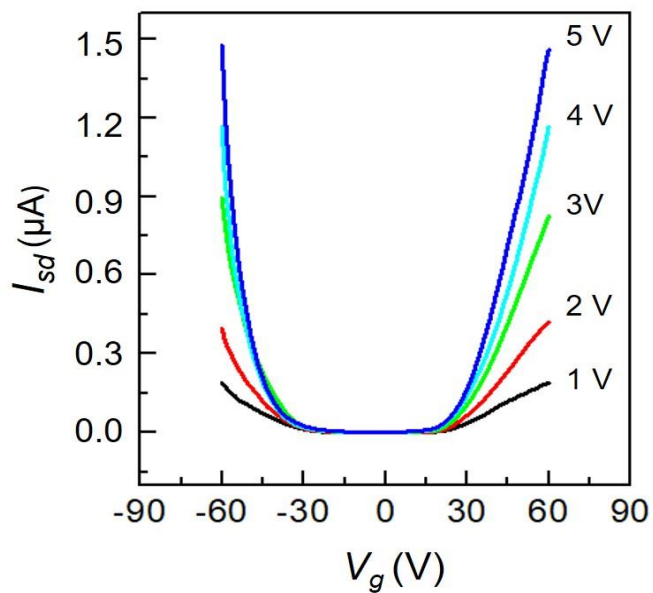
Figure S6. The transfer curves of the ReSe₂-LET with ℓ_c = 15 μm on an h-BN/SiO₂ (300 nm thick)/Si substrate.

**S8. Detection of Near-Infrared Electroluminescence**

The measurements of the electroluminescence (EL) emitted from the ReSe$_2$-LET device were performed inside a dark Faraday cage under ambient conditions. The electrically shielded Faraday cage was electrical ground, resistant to electromagnetic interference, and maintained at a relative humidity of 10% to prevent the Ge detector's window from fogging. The ReSe$_2$-LET device was modulated at $f_m = 19$ kHz using the square wave generated from a function generator (Stanford Research Systems, DS335). The EL from ReSe$_2$-LET was filtered by a bandpass filter (BPF, Edmund Optics; with the central wavelength at 975 ± 25 nm and the transmission efficiency of ~68% at 984 nm) and detected by a Ge detector (Teledyne Judson, J16D series Nitrogen Cooled) sensitive to the NIR light at 800−1650 nm. The Ge detector has an active detection element (5 mm in diameter) with the maximal responsivity of 0.5 A/W at 1300 nm. The frequency-modulated signals (at $f_m = 19$ kHz) were collected by the Ge detector and fed into a lock-in amplifier (Stanford Research Systems, SR830 DSP), where the instruments were interfaced and controlled with the LabVIEW program. As displayed in **Figure S7**, the positions of the ReSe$_2$-LET device and the Ge detector were adjusted separately with three-axis XYZ micropositioner stages. When a BPF or a linear polarizer was used in the measurements, the optical component (i.e., BPF/polarizer) was inserted between the Ge detector and the ReSe$_2$-LET device along the optical path of the emitted EL. The separation between the Ge detector and the ReSe$_2$-LET device was ~20 mm.
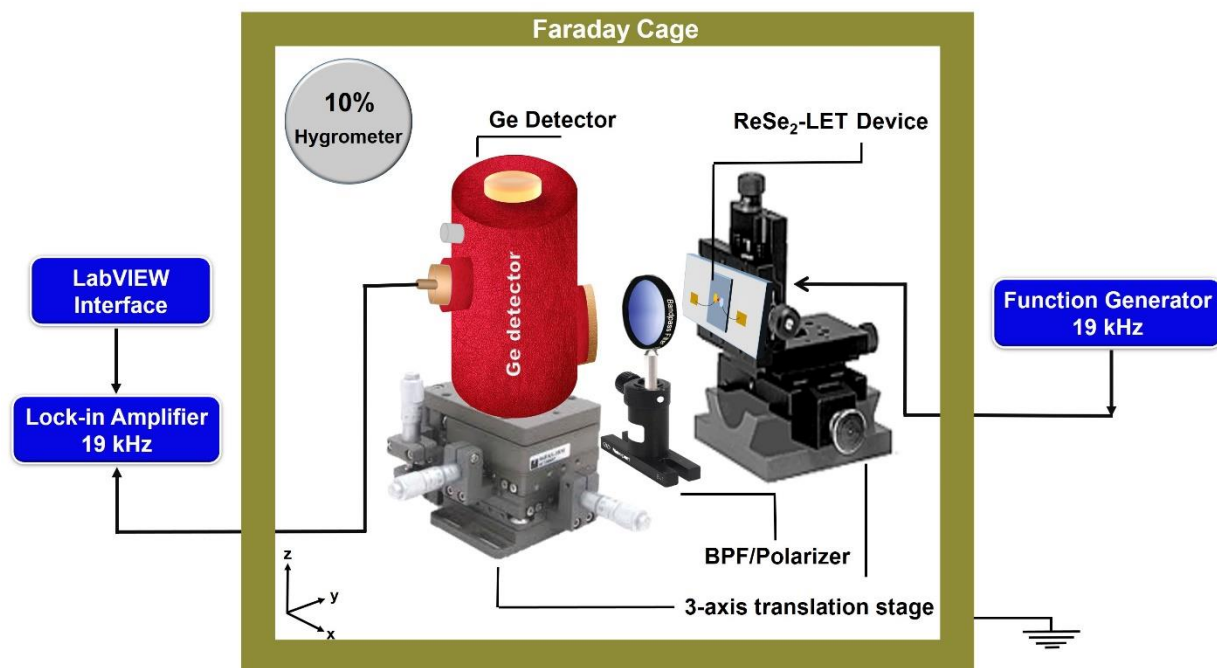
Figure S7. To detect the EL from ReSe$_2$-LET, the experimental setups, including an ReSe$_2$-LET device, a Ge detector, a BPF/polarizer, and a lock-in amplifier, were placed inside a Faraday cage maintained at a relative humidity of ~10%. The position of the ReSe$_2$-LET device relative to the Ge detector was adjusted with three-axis XYZ micropositioner stages.

S9. Optimization of the Modulation Frequency

We tried to obtain the maximal output of I_{ph}, excited by the EL from ReSe$_2$-LET ($\ell_c =$ 0.9 μm, $V_b = 1$ V, and $V_g = 0$ V), by varying the modulation frequency (f_m) of the lock-in amplifier used. As shown in **Figure S8**, the I_{ph} was measured with a stepwise change of f_m from 101 kHz to 1 Hz. While I_{ph} increased as f_m increased from 1 Hz to 10 kHz, I_{ph} started to decrease when f_m was further escalaed from 50 kHz to 101 kHz. Around $f_m \sim 25$ kHz, the maximal output of I_{ph} was found. We, therefore, fine-tuned f_m from 10 kHz to 25 kHz at every 1 kHz interval to obtain the maximal I_{ph} at $f_m = 19$ kHz as displayed in the inset of **Figure S8** (also shown in **Figure 3b** of the main text).
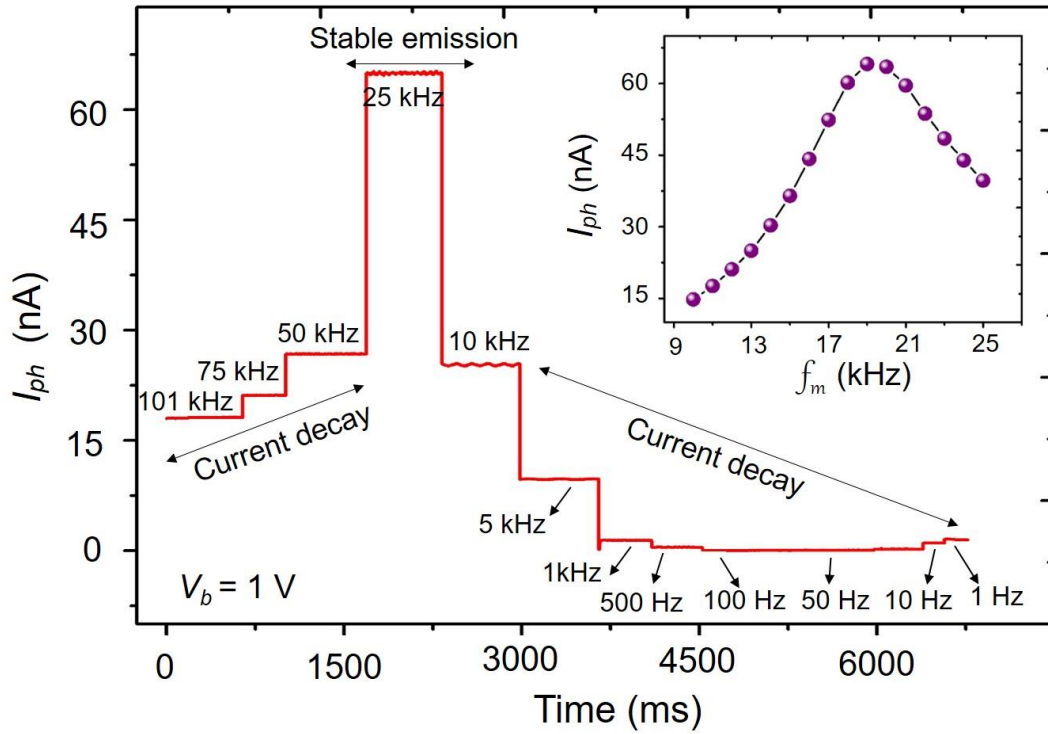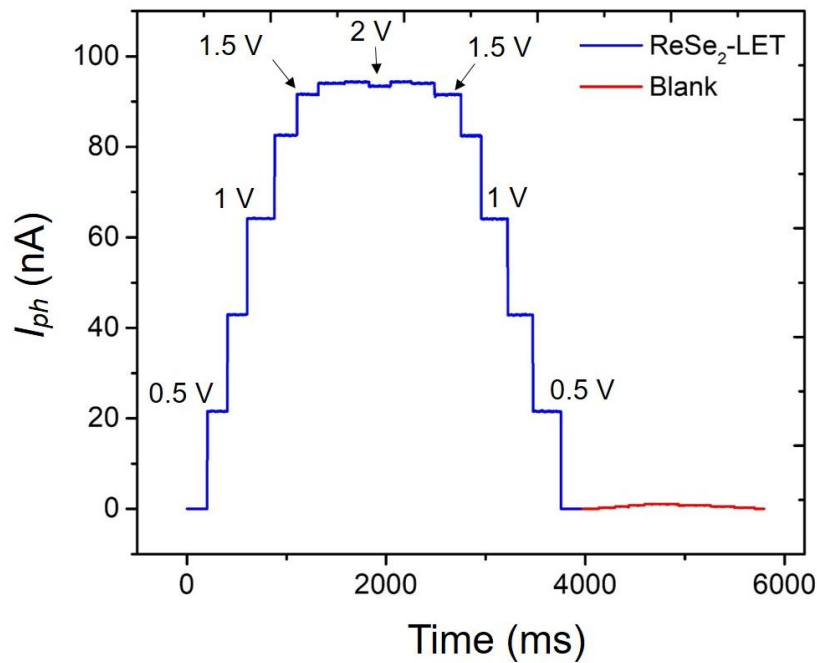

Figure S8. The I_{ph} excited by the EL from ReSe$_2$-LET was investigated by varying f_m with a stepwise change from 101 kHz to 1 Hz. Since the maximal I_{ph} was detected around $f_m \sim 25$ kHz, we fine-tuned f_m from 10 kHz to 25 kHz at every 1 kHz interval to obtain the maximal I_{ph} at $f_m = 19$ kHz (as shown in the inset as well as **Figure 3b** of the main text). In this test, the ReSe$_2$-LET device of $\ell_c = 0.9$ μm was operated at $V_b = 1$ V and $V_g = 0$ V.

S10. Optimization of the Bias Voltage

With an ReSe$_2$-LET device of $\ell_c = 0.9$ μm operated at $f_m = 19$ kHz, we tested the output of I_{ph} by applying different V_b at 0–2 V. In **Figure S9**, the detected I_{ph} increases monotonically at low V_b and becomes saturated at $V_b > 1.5$ V. The trend of the observed V_b-dependent I_{ph} was further confirmed by the reverse scan of V_b from 2 to 0 V. The measured I_{ph} vs. V_b plot is displayed in **Figure 3b** of the main text.

To confirm that the detected I_{ph} was excited genuinely by the NIR EL from ReSe$_2$-LET, we conducted a control test with a device without the ReSe$_2$ conducting channel (i.e., a blank device has electrodes only). The red trace on (the right-hand side of) **Figure S9** shows a negligible I_{ph} response from the use of this blank device even operating at $V_b = 0$–2 V, verifying that the I_{ph} was truly generated by the ReSe$_2$-LET-emitting EL.

Figure S9. (blue trace) The I_{ph} excited by the EL from ReSe$_2$-LET ($\ell_c = 0.9$ μm and $f_m = 19$ kHz) was measured when the LET device was operated stepwise at $V_b = 0$–2 V. (red trace) For comparison, the I_{ph} of a blank device (without the ReSe$_2$ conducting channel) was also measured to be almost negligible at $V_b = 0$–2 V.

S11. Distance-Dependent Photocurrent from an ReSe₂-LET
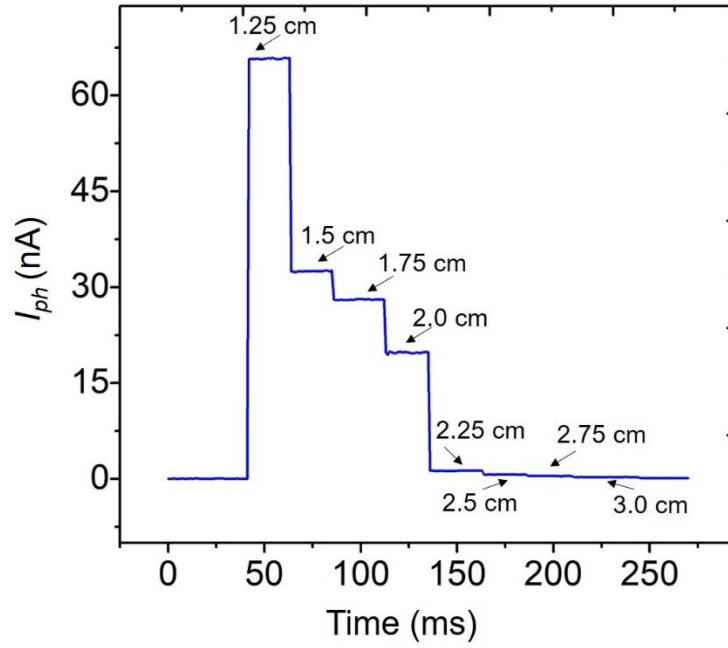
Figure S10. The I_{ph} excited by the EL from ReSe₂-LET (ℓ_c = 0.9 µm, V_b = 1 V, and f_m = 19 kHz) was measured as a function of the distance from the LET device. The distance was varied from 12.5 to 30 mm with a three-axis XYZ micropositioner stage at every 2.5 mm interval.
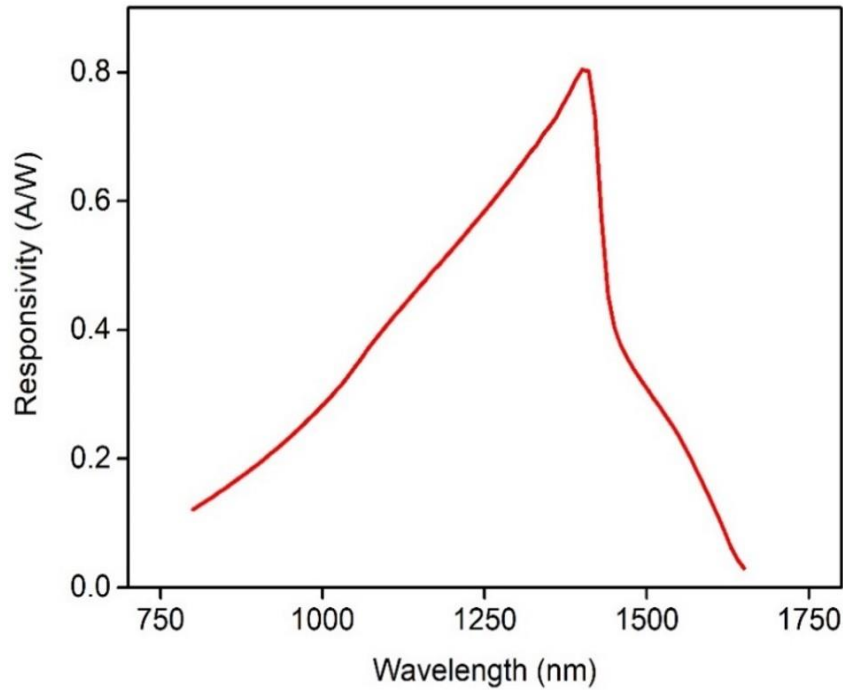
S12. Wavelength-Dependent Responsivity of a Ge Detector

In **Figure S11**, the responsivity of the Ge detector (0.2630 A/W at 980 nm) is determined based on the wavelength-dependent responsivity curve of the Ge detector used in the measurements. The quantum yield (q_p) of the Ge detector was calculated by

$$q_p = \frac{Rhc}{e\lambda} \tag{S5}$$

where R is the responsivity of the detector, h is the Plank's constant, c is the speed of light, e is the elementary charge, and λ is the wavelength of the emission at 980 nm. Substituting these values into Eq. (S5), we obtained

$$q_p = \frac{0.2630 \times 6.626 \times 10^{-34} \times 3.0 \times 10^8}{1.602 \times 10^{-19} \times 980 \times 10^{-9}} = 0.333.$$

Figure S11. The quantum yield of the NIR EL from ReSe$_2$-LET was calculated with the measured wavelength-dependent responsivity of the Ge detector.

S13. Characteristic Parameters of the EL from ReSe₂-LET

(A) Radiant Power

Assuming that all of the EL emitted from the ReSe₂-LET device fell on the active detection element of the Ge detector, the radiant power (Φ) received by the Ge detector can be calculated by[S12]

$$\Phi = \left[\frac{I_{Ph}}{q_p e}\right] \frac{hc}{\lambda} \tag{S6}$$

where $I_{ph} = 91.6$ nA is the photocurrent excited by the EL from ReSe₂-LET ($\ell_c = 0.9$ μm, $V_b = 1.5$ V, and $f_m = 19$ kHz) and detected by the Ge detector, $q_p = 0.333$ is the quantum yield of the Ge detector (**Section S12**), e is the elementary charge, h is the Plank's constant, c is the speed of light, and λ is the wavelength of the detected emission at 980 nm. Substituting these values into Eq. (S6), we obtained

$$\Phi = \frac{91.6\times10^{-9} \times 6.626 \times10^{-34} \times 3.0\times10^{8}}{0.333 \times 1.602 \times10^{-19} \times 980\times10^{-9}} = 3.48 \times 10^{-7} \text{ W}.$$

(B) Irradiance

The irradiance (P) is defined as the power produced by a light source per unit area.[S13]

$$P = \frac{\Phi}{4\pi r^2} \tag{S7}$$

where Φ is the radiant power and $r = 1.25$ cm is the distance between the ReSe₂-LET device and the Ge detector. Using the radiant power (Φ) value obtained above, we computed the irradiance of an ReSe₂-LET ($\ell_c = 0.9$ μm, $V_b = 1.5$ V, and $f_m = 19$ kHz) to be

$$P = \frac{3.48 \times10^{-7}}{4\times3.14 \times(1.25\times10^{-2})^2} = 1.77 \times 10^{-4} \text{ W/m}^2 = 0.177 \text{ fW/μm}^2.$$

(C) Radiant Intensity

The radiant intensity (I) of a light source is defined as the light emitted from a source per unit solid angle in a specified direction. We calculated[S13]

$$I = \frac{\Phi}{\Omega} \tag{S8}$$

where Φ is the radiant power and Ω is the solid angle of emission. Assuming that the incident emission on the Ge detector is approximately in a circular shape, the solid angle is calculated by

$$\Omega = \frac{A_{circle}}{r^2} = \frac{\pi\, a^2}{r^2} = 0.126 \text{ sr.} \tag{S9}$$

where $a = 2.5$ mm is the radius of the active detection element of the Ge detector and $r = 1.25$ cm is the distance between the ReSe$_2$-LET device and the Ge detector. The solid angle is calculated to be 0.126 sr from Eq. (S9). Substituting this value into Eq. (S8),

$$I = \frac{3.48 \times 10^{-7}}{0.126} = 2.77 \times 10^{-6} \text{ W/sr.}$$

(D) Efficiency

The power-conversion efficiency of an ReSe$_2$-LET can be estimated by the ratio of the output power (radiant power, P_o) of the LET device to the electrical input power (P_{in} = *input current* $\times$ *bias voltage*). Therefore, the efficiency (η) of the device is given by

$$\eta = P_o/P_{in} = \frac{3.48 \times 10^{-7}}{7.27 \times 10^{-7} \times 1.5} = 0.319 \times 100\% = 31.9 \%$$

References

[S1]   R. D. Nikam, P. A. Sonawane, R. Sankar, Y. T. Chen, *Nano Energy* **2017**, *32*, 454.

[S2]   X. Li, L.Yang , M. Si , S. Li , M. Huang , P. Ye , Y. Wu. *Adv. Mater.* **2015**, *27*, 1547-1552.

[S3]   N. Ma, D. Jena, *Phys. Rev. X* **2014**, *4*, 011043.

[S4]   V. Perebeinos, P. Avouris, *Phy. Rev. B*, **2010**, *81*, 195442.

[S5]   N. Haratipour, M. C. Robbins, and S. J. Koester, *IEEE Elec. Dev. Lett.* **2015**, 36, 15012854.

[S6]   Z. Yu, Z.-Y. Ong, Y. Pan, Y. Cui, R. Xin, Y. Shi, B. Wang, Y. Wu, T. Chen, Y.-W. Zhang, G. Zhang, X. Wang, *Adv. Mater.* **2016**, *28*, 547-552.

[S7]   Y. Cui , R. Xin , Z. Yu , Y. Pan , Z.-Y. Ong , X. Wei , J. Wang , H. Nan , Z. Ni , Y. Wu , T. Chen, Y. Shi, B. Wang, G. Zhang, Y.-W. Zhang, X. Wang, *Adv. Mater.* **2015**, 27, 5230–5234.

[S8]   A. Konar, T. Fang, D. Jena, *Phy. Rev. B*, **2010**, *82*, 115452.

[S9]   C.Wang, F.Yang and Y. Gao, Nanoscale Adv., **2020**, *2*, 4323–4340.

[S10]   S. Q. Wang, G. D. Mahan, *Phys. Rev. B,* **1972**, *6*, 4517-4524.

[S11]   H. Zhong, Z. Zhang, H. Xu, C. Qiu, L.-M. Peng, *AIP Adv.* **2015**, *5*, 057136.

[S12]   C. Manilerd, International Physics Olympiads: Problems and Solutions from 1967-1995, Rangsit University Press, **1995**.

[S13]   Bahaa E A Saleh; Malvin Carl Teich, Fundamentals of Photonics 3rd Edition, John Wiley & Sons, **2019**.